

A Two-Dimensional Model of Chemical Vapor Infiltration With Radio Frequency Heating

Vikas Midha and Demetre J. Economou*

Plasma Processing Laboratory, Department of Chemical Engineering, University of Houston,
Houston, Texas 77204-4792, USA

ABSTRACT

A comprehensive, two-dimensional, self-consistent model was developed and used to simulate chemical vapor infiltration of fiber-reinforced composite materials with radio frequency heating. The model included equations for energy transport, multicomponent mass transport, and pore structure evolution, coupled to Maxwell's equations to determine self-consistently the power absorbed by the preform from a radio frequency induction coil. The model equations were solved by a finite element method to study carbon chemical vapor infiltration in a cylindrical carbon preform. Simulations for a constant absorbed power showed that densification of the preform proceeds in an "inside out" manner, first in the radial direction and subsequently in the axial direction, for the aspect ratio studied. The power density distribution in the preform evolves in a complex manner as densified regions absorb more energy with increased densification. This may result in thermal runaway during the infiltration process and entrapment of porosity in the interior of the preform. Comparison of simulated results with reported experimental data showed semiquantitative agreement of important trends. A more accurate description of material properties is required for a quantitative match with the data.

Introduction

Chemical vapor infiltration (CVI) has emerged as one of the leading techniques for the fabrication of fiber-reinforced composite materials. The conventional isothermal CVI process consists of diffusion of reactant gases into a porous preform at constant temperature. Reactants undergo chemical reactions on the surface of the pores to deposit solid material thereby filling the pores. This process allows the near-net-shape production of composite materials of complex geometries without structural damage to the initial preform. The major disadvantage of the isothermal process, however, is that extremely long processing times are required. Processing times can extend to days or weeks depending on the preform thickness. If the operating temperature is increased, diffusional limitations force the pores at the surface of the preform to densify at a faster rate than the pores in the interior. This nonuniform densification eventually leads to premature closure of the pores at the surface of the preform without completely filling the inner void space.

A promising modification to the conventional isothermal CVI is to combine chemical vapor infiltration with volumetric heating of the preform. Volumetric heating with cooling at the boundaries produces an "inverted" temperature gradient. As the reactant gas diffuses into the preform, this temperature gradient favors higher rates of reaction in the interior of the preform as opposed to the surface. Thus, CVI with volumetric heating has the potential to produce rapid infiltration with an "inside-out" densification pattern. As opposed to other temperature-gradient processes proposed in the literature,^{1,2} volumetric heating does not impose restrictions on the geometry of the preform and preserves one of the primary advantages of CVI.

Volumetric heating may be accomplished by inducing electromagnetic fields in the preform either in a conventional microwave oven or by using a radio frequency (RF) induction coil. The frequency of operation is governed by the electrical conductivity of the material and the thickness of the preform to be heated. The penetration depth of the electromagnetic fields within the preform can be increased by lowering the operating frequency. Microwave heating is limited to the processing of relatively thin preforms and materials of relatively low electrical conductivity. Devlin *et al.* reported the densification of SiC cloth lay-ups in a conventional 700 W multimode microwave oven at a frequency of 2.45 GHz.³ For thicker preforms and/or materials which are relatively good conductors, volumetric heating at lower frequencies may be necessary. Sugiyama and Ohzawa showed that infiltration of carbon

preforms with SiC could be achieved using an RF coil at 400 kHz.⁴ Golceki *et al.* reported the densification of carbon disks using RF heating at frequencies of 4.9 to 8.6 kHz and power in the range 8.8 to 13.2 kW.⁵⁻⁸ A recent study by Devlin *et al.* showed the infiltration of three-dimensional carbon preforms using an RF heating supply of 6 kW at 50 kHz.⁹

Modeling studies of CVI with volumetric heating reported in the literature are restricted to one-dimensional models (1D). Gupta and Evans modeled the infiltration of SiC at microwave frequencies and showed the existence of "inverted" thermal gradients which could be exploited for CVI.¹⁰ Morell *et al.* modeled the infiltration of carbon preforms by representing volumetric heating as a constant heat source term in the energy balance.^{11,12} They showed the existence of a critical value of power above which accessible porosity is trapped inside the composite. Various power modulation schemes and pulsed power were proposed to achieve rapid densification without entrapment of accessible porosity. In a later study on the infiltration of SiC with microwave heating, Morell *et al.* accounted for the variation of power across the thickness of the preform by solving Maxwell's equations for the electric field.¹³

Although 1D models are adequate for a preliminary evaluation of the process, 2D models are necessary to account for the finite geometry of the preform. Important approximations in the physical description of the process introduced by 1D models can be eliminated by 2D models. For instance, during the infiltration of a cylindrical preform, cooling occurs at all boundaries. Thus, "inverted" temperature gradients will be produced in both radial and axial directions, and the total temperature gradient will dictate the densification pattern in the preform. Similarly, pore space in the preform may appear to be entrapped due to diffusional limitations in one dimension, but it may actually be accessible to the reactant gas from other directions. Therefore, 1D models will tend to overestimate the entrapped porosity during the infiltration process.

Although 2D models for CVI with volumetric heating have not been reported in the literature, various models for other temperature-gradient CVI processes are available.^{2,14-16} All these studies, however, are based on simple models for mass transport; either simple binary diffusion or forced viscous flow of reactant gas in the preform. However, studies by Sotirchos¹⁷ and Morell *et al.*¹¹⁻¹³ indicate that multicomponent diffusion, Knudsen diffusion, and viscous flow may all play an important role in CVI applications, depending on the operating conditions.

In the present study, a comprehensive two-dimensional model was developed for the simulation of CVI with volumetric heating. The model incorporated an energy balance

* Electrochemical Society Active Member.

with RF induction heating, multicomponent mass transport of the gaseous species within the preform, and a solid balance for the evolution of porosity. Maxwell's equations were solved self-consistently with the porosity evolution not only to determine the two-dimensional distribution of the electromagnetic fields in the preform, but also to evaluate how the power density from the fields varies during the densification process. The model equations were solved by using the Galerkin finite element method to simulate the infiltration of a cylindrical carbon preform by the decomposition of methane. Results from the simulations were compared to those reported in a recent experimental study.

Model Formulation

A schematic of the RF induction heating apparatus and CVI reactor considered in this study is shown in Fig. 1. The cylindrical carbon preform is placed coaxially in a cylindrical quartz reactor. An RF induction coil surrounds the reactor and is used to provide volumetric heating of the preform to desired temperatures. The gaseous reactant mixture flows continuously in the reactor, maintaining a constant species concentration at the surface of the preform. Gaseous precursors diffuse into the porous preform and chemically react at the elevated temperatures to deposit solid within the pores. The CVI reactor and RF induction coil are all enclosed in a metallic chamber to contain radiation.

Due to the different spatial domains encompassed by the electromagnetic and CVI phenomena, the model was divided into two modules: (i) an electromagnetic (EM) module which evaluated the electric fields in the entire chamber surrounded by the metallic enclosure, the main output being the power deposited in the preform by the induction coil; (ii) a CVI module which solved the relevant mass and energy balances describing the infiltration process on the geometry of the preform alone. The two modules were coupled to each other by the power density (calculated by the EM module) which affects the preform temperature and the evolving porosity of the preform (calculated by the CVI module) which affects the absorbed power.

An extension of this study would include a third module for the reactor space (outside the preform) through which gas flow and reaction takes place. This module would account, for example, for reactant depletion as the gas flows downstream. This module is not necessary in the present work since it was assumed that the gas species density at the surface of the preform is the same as in the feedstock gas.

In the following section, the governing equations describing the EM and CVI modules are presented. The form of the equations shown here enabled a convenient

Galerkin finite-element formulation for numerical solution of the equations.

Electromagnetic module.—The EM fields due to the induction coil obey Maxwell's equations. It was assumed that the frequency of the RF fields is high enough that the temperature of the preform follows only the time-averaged value of the power deposited by the fields. This assumption is justified later by comparing the characteristic time for heat transfer with the period of the oscillations of the electromagnetic fields. Under these conditions, Maxwell's equations may be solved in the frequency domain with a time-harmonic dependence of the form $e^{-j\omega t}$. Assuming linear, isotropic electrical properties of the preform material, Maxwell's equations may be simplified to the following form¹⁸

$$\nabla \times \mathbf{E} = j\omega\mu_0\mathbf{H} \quad [1]$$

$$\nabla \times \mathbf{H} = -j\omega\epsilon_0 K_c \mathbf{E} + \mathbf{J}^i \quad [2]$$

$$\epsilon_0 \nabla \cdot (K \mathbf{E}) = \rho_v \quad [3]$$

$$\nabla \cdot \mathbf{H} = 0 \quad [4]$$

where \mathbf{J}^i represents the impressed current density, ρ_v is the volumetric charge density, and K is the relative permittivity of the material. K_c represents the complex relative permittivity including the contribution of the electrical conductivity of the material. Equations 1 and 2 may be combined to give the vector wave equation

$$-\nabla \times \nabla \times \mathbf{E} + \frac{\omega^2}{c^2} K_c \mathbf{E} = -j\omega\mu_0 \mathbf{J}^i \quad [5]$$

The impressed current, \mathbf{J}^i , follows the contour of the induction coil and is distributed in three-dimensional space around the reactor. In addition, at high operating frequencies, the current varies along the length of the coil due to capacitive coupling between the coil, the metal boundaries of the enclosure, and the dielectric material.¹⁹ A rigorous calculation, therefore, would require a detailed description of the geometry of the coil and the solution of the full three-dimensional form of Eq. 5 for E_θ , E_r , and E_z .

A simplification may be introduced, however, by representing the geometry of the coil as a set of discrete loops of impressed current.²⁰ Within each loop, the current is approximated as constant, equal to the average value of the current at the beginning and end of the loop. The impressed current \mathbf{J}^i , therefore, has only an azimuthal component and the resultant electric field is azimuthally symmetric. Combined with the boundary conditions which require the tangential component of the electric field to vanish at the metal enclosure, Eq. 5 implies that the resultant electric field is also directed only in the azimuthal direction. Eq. 5 may be simplified to

$$\nabla^2 E_\theta + \frac{\omega^2}{c^2} K_c E_\theta = -j\omega\mu_0 J_\theta^i \quad [6]$$

or, in expanded form as

$$\frac{1}{r} \frac{\partial}{\partial r} \left(r \frac{\partial E_\theta}{\partial r} \right) + \frac{\partial^2 E_\theta}{\partial z^2} + \frac{E_\theta}{r^2} + \frac{\omega^2}{c^2} K_c E_\theta = -j\omega\mu_0 J_\theta^i \quad [7]$$

The EM module can account for variations of the current from loop-to-loop due to capacitive coupling. However, an additional simplification may be introduced at low frequencies by neglecting capacitive losses of the coil current. Capacitive coupling becomes significant when the length of the coil approaches a quarter wavelength at the operating frequency.¹⁹ For a coil length of ~100 cm, this corresponds to a frequency of 5 MHz. Since typical operating frequencies for carbon-carbon CVI are in the range 10 to 50 kHz, this assumption is justified. Thus, for the present study, the current was assumed to be the same for each and every loop of the coil. The value of the current was continuously adjusted to maintain constant total power deposition within the preform.

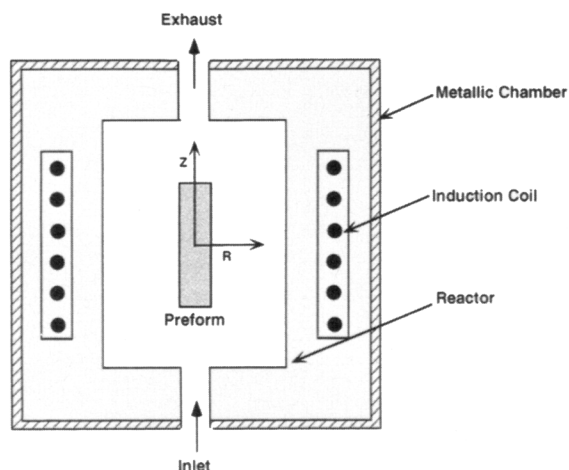


Fig. 1. Schematic of CVI reactor and RF induction coil studied.

Once the electric field distribution in the 2D enclosure is known, the time-averaged value of the power density deposited in the preform due to ohmic heating may be evaluated by

$$W = \frac{1}{2} \sigma^e |\mathbf{E}|^2 \quad [8]$$

where W is the power density and σ^e is the effective electrical conductivity of the composite material, and $|\mathbf{E}|^2$ is the square of the modulus of the electric field. Since the electrical conductivity of the gaseous phase is negligible, σ^e is modeled by a simple linear dependence of the form

$$\sigma^e = \sigma_s(1 - \epsilon) \quad [9]$$

where σ_s is the electrical conductivity of the solid and ϵ is the porosity of the composite material.

CVI module.—The chemical vapor infiltration process is characterized by the time evolution of the temperature, pressure, mole fractions of the gaseous species, and preform porosity. These quantities are evaluated from the energy balance and mass balance equations in the CVI module. The formulation of the governing equations is kept general enough to allow the description of various other CVI processes such as isothermal, forced flow, and pressure-pulsed CVI along with CVI with volumetric heating considered in this study.

Energy balance.—An overall energy balance is constructed by assuming negligible heat-transfer resistance between the preform fibers and the gaseous mixture. The unsteady-state energy balance for the gas-permeated preform is given by

$$\frac{\partial h^e}{\partial t} + \nabla \cdot \mathbf{N}_H = (1 - \epsilon)W \quad [10]$$

where h^e is the effective partial molar enthalpy of the gas-permeated preform (solid plus gas), \mathbf{N}_H is the enthalpy flux per unit cross section of the porous medium, and W is the power adsorbed per unit volume due to induction heating. Since the fields directly heat the solid phase only, the source term in Eq. 10 is appropriately weighted by the solid fraction. The heat liberation due to chemical reactions is assumed to be negligible compared to the induction heating term. The partial molar enthalpy, h^e , may be approximated by the following expression for moderately low pressures

$$h^e = \epsilon \sum_{i=1}^{N_c} C_i C_{p_i} (T - T_a) + (1 - \epsilon) C_s C_{p_s} (T - T_a) \quad [11]$$

where C_i is the concentration of species i , C_{p_i} is its molar heat capacity, C_s is the molar concentration of the solid species, C_{p_s} is the molar heat capacity of the solid, and T_a is the ambient temperature. If the contribution of the specific heat of the gas is neglected in comparison to the solid, substitution of Eq. 11 into Eq. 10 yields

$$(1 - \epsilon) C_s C_{p_s} \frac{\partial T}{\partial t} - C_s C_{p_s} (T - T_a) \frac{\partial \epsilon}{\partial t} + \nabla \cdot \mathbf{N}_H = (1 - \epsilon)W \quad [12]$$

The enthalpy flux in the porous medium, \mathbf{N}_H , is due to convection of the components of the gaseous mixture and heat conduction within the preform

$$\mathbf{N}_H = \sum_{i=1}^{N_c} \mathbf{N}_i C_{p_i} (T - T_a) - k^e \nabla T \quad [13]$$

where \mathbf{N}_i is the molar flux of the i th species and k^e is the effective conductivity of the gas-permeated preform. The effective thermal conductivity is related to the preform porosity by the relation

$$k^e = k_s(1 - \epsilon^2) + k_g \epsilon^2 \quad [14]$$

where k_s and k_g are the thermal conductivities of the solid and gaseous phase, respectively.

Mass balance for the chemical species in the gaseous phase.—A gaseous phase is considered consisting of N_c components with N_r chemical reactions taking place. The unsteady-state differential mass balance for species i is given by

$$\frac{\partial(\epsilon C_i)}{\partial t} + \nabla \cdot \mathbf{N}_i = \sum_{r=1}^{N_r} \nu_{ir} R_r \quad [15]$$

where R_r is the (molar) rate of the r th reaction per total volume of the porous medium (solid plus gas) and ν_{ir} is the stoichiometric coefficient of the i th species in the r th reaction. Using the ideal gas law $p = CRT$ and the relation $C_i = x_i C$, Eq. 15 may be expanded to give

$$-\left(\frac{x_i \epsilon p}{RT^2}\right) \frac{\partial T}{\partial t} + \left(\frac{x_i \epsilon}{RT}\right) \frac{\partial p}{\partial t} + \left(\frac{x_i p}{RT}\right) \frac{\partial \epsilon}{\partial t} + \left(\frac{\epsilon p}{RT}\right) \frac{\partial x_i}{\partial t} + \nabla \cdot \mathbf{N}_i = \sum_{r=1}^{N_r} \nu_{ir} R_r \quad [16]$$

In addition, the mass balance equations for individual species given by Eq. 15 may be summed over the total number of gaseous species, N_c , to give an overall mass balance for the gaseous phase

$$\frac{\partial(\epsilon C)}{\partial t} + \nabla \cdot \mathbf{N}_T = \sum_{i=1}^{N_c} \sum_{r=1}^{N_r} \nu_{ir} R_r \quad [17]$$

Equation 17 may be expressed in terms of the system pressure as

$$-\frac{\epsilon p}{RT^2} \frac{\partial T}{\partial t} + \frac{\epsilon}{RT} \frac{\partial p}{\partial t} + \frac{p}{RT} \frac{\partial \epsilon}{\partial t} + \nabla \cdot \mathbf{N}_T = \sum_{i=1}^{N_c} \sum_{r=1}^{N_r} \nu_{ir} R_r \quad [18]$$

This pressure equation is critical for modeling CVI processes where gas flow is important, including forced-flow and pulsed-pressure CVI.

The transport of the gaseous species within the porous medium occurs by a combination of molecular diffusion, Knudsen diffusion, and viscous flow. For dilute gaseous mixtures at relatively high operating pressures, a simple binary diffusion description may suffice. However, typical mixtures used for CVI processes are not dilute, and multi-component diffusion effects can become significant. When the operating pressure is low enough, the mean free path of the molecules becomes comparable to the radius of the pores and Knudsen diffusion becomes significant. Similarly, under conditions with large pressure gradients, viscous flow of the gaseous reactant within the pores may become dominant. The contribution of all these mechanisms is accounted in the present formulation by evaluating molar fluxes by the Dusty Gas model.²¹

The Dusty Gas model divides the total molar flux of species i into diffusive and convective components

$$\mathbf{N}_i = \mathbf{J}_i + x_i \mathbf{N}_T \quad [19]$$

The diffusive component of flux \mathbf{J}_i is related to the gradient of its mole fraction and the total pressure by

$$\sum_{j=1}^{N_c} \frac{x_j \mathbf{J}_j - x_i \mathbf{J}_i}{\Delta_{ij}} = \frac{-p}{RT} \nabla x_i - \frac{x_i}{RT} \left(1 - \frac{1}{D_i^e} \frac{1}{\sum_{s=1}^{N_c} \frac{x_s}{D_s^e}} \right) \nabla p \quad [20]$$

where

$$\frac{1}{\Delta_{ij}} = \frac{1}{D_{ij}^e} + \frac{1}{D_i^e D_j^e \sum_{s=1}^{N_c} \frac{x_s}{D_s^e}} \quad [21]$$

Here, D_{ij}^e and D_i^e denote the effective binary and Knudsen diffusion coefficients of species i in the porous medium, respectively. Equation 20 provides $N_c - 1$ linearly independent relations for the diffusive fluxes of N_c components in the gaseous phase. The additional relation between the diffusive fluxes is given by

$$\sum_{i=1}^{N_c} \mathbf{J}_i = 0 \quad [22]$$

which may be combined with Eq. 20 to solve for the diffusive flux of each and every species. Once the diffusive components are known, the total flux \mathbf{N}_T due to diffusion and viscous flow of the multicomponent mixture is given by

$$\mathbf{N}_T = \frac{\sum_{s=1}^{N_c} \frac{\mathbf{J}_s}{D_s^e}}{\sum_{s=1}^{N_c} \frac{x_s}{D_s^e}} - \frac{1}{RT} \left[\frac{Bp}{\mu} + \frac{1}{\sum_{s=1}^{N_c} \frac{x_s}{D_s^e}} \right] \nabla p \quad [23]$$

where B is the permeability of the porous medium and μ is the viscosity of the gas mixture. Equations 16 to 23 suffice to solve for the concentration profiles of all species and the pressure distribution in the preform.

The mass diffusivities of the chemical species were estimated at a reference temperature using the Chapman-Enskog theory.²² Variations in the diffusivities due to temperature, pressure, and pore structure are given by

$$D_{ij}^e = D_{ij}^{\text{ref}} \left(\frac{p^{\text{ref}}}{p} \right) \left(\frac{T}{T^{\text{ref}}} \right)^{1.65} S_1 \quad [24]$$

for binary diffusivities, and

$$D_i^e = D_i^{\text{ref}} \left(\frac{T}{T^{\text{ref}}} \right)^{1.65} S_2 \quad [25]$$

for Knudsen diffusivities. S_1 and S_2 represent pore structure parameters dependent on the particular pore structure model used.

The pore structure of the three-dimensional carbon preform was represented by a network of uniformly sized cylindrical capillaries of radius r_p .¹⁷ The radius of the capillaries evolves with densification of the preform as

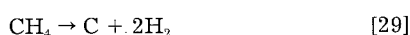
$$r_p = r_p^{\text{ref}} \sqrt{\frac{\ln(1 - \epsilon)}{\ln(1 - \epsilon_0)}} \quad [26]$$

with ϵ_0 representing the initial porosity of the preform. Given the radius of the pore, the permeability of the porous medium, and the variation in the pore structure parameters (S_1 and S_2) are given by

$$B = \frac{\epsilon}{3} \left(\frac{r_p^3}{8} \right) \quad [27]$$

$$S_1 = \frac{\epsilon}{3} \text{ and } S_2 = \frac{\epsilon}{3} \left(\frac{r_p}{r_p^{\text{ref}}} \right) \quad [28]$$

Reaction kinetics.—The deposition of carbon by the decomposition of methane was considered. The complete mechanism and kinetics of methane decomposition under CVI conditions are still not well understood. Several experimental studies suggest that the rate of decomposition is limited by the initial rupture of the C-H bond in methane and is first order in the methane concentration. However, it is expected that surface chemistry should play a decisive role in CVI where the surface-to-volume ratio is very high. In the absence of kinetic information, a simplified reaction of the form



was assumed with the rate of reaction given by

$$R_{\text{CH}_4} = k_1 C_{\text{CH}_4} \exp[-E_1/(RT)] \quad [30]$$

In Eq. 30, k_1 is the rate constant and E_1 is the activation energy of the reaction. The values of these parameters were taken as 2.24×10^{14} 1/s and 3.64×10^5 J/mol, respectively.^{11,12} A more detailed kinetic model including precursor adsorption, surface reaction, and product desorption is the focus of future work.

Overall mass balance for the solid phase.—The evolution of preform porosity was described by a mass balance for the solid phase of the form

$$\frac{\partial \epsilon}{\partial t} = -\frac{M_s}{\rho_s} \sum_{r=1}^{N_R} v_{sr} R_r \quad [31]$$

where M_s is the molecular weight of the deposited solid, ρ_s is the density of the deposited solid, and v_{sr} is the stoichiometric coefficient of the solid species in the r th reaction.

Initial and boundary conditions.—Initially the preform and the gas mixture are both assumed to exist at ambient conditions

$$T = T_a, x_i = 0, p = p_a, \text{ and } \epsilon = \epsilon_0 \quad [32]$$

The initial porosity of the preform ϵ_0 was assumed uniform. To complete the formulation of the model equations, boundary conditions are also required. At the exterior surface of the preform, heat is lost due to convection and radiation to the surroundings. This may be expressed as

$$\mathbf{n} \cdot \mathbf{N}_H = h(T - T_a) + se(T^4 - T_a^4) \quad [33]$$

where \mathbf{n} denotes a unit vector normal to the surface of the preform, h is the heat transfer coefficient, s is the Stefan-Boltzmann constant, and e is the emissivity of the material. The convection term is significant only at lower temperatures. Convective losses are quickly overpowered by radiation losses once relatively high temperatures are attained. Similarly, a boundary condition of the form

$$x_i = x_a \quad [34]$$

is valid for the species mass balances if the external mass-transfer resistance is negligible. For the overall mass balance, the pressure at exterior surfaces was assumed to be maintained at a specified constant value

$$p = p_a \quad [35]$$

On boundaries with symmetry, it is required that the total heat flux, the mass flux of each species, and the total mass flux be zero, *i.e.*

$$\mathbf{n} \cdot \mathbf{N}_H = 0, \mathbf{n} \cdot \mathbf{N}_i = 0 \text{ and } \mathbf{n} \cdot \mathbf{N}_T = 0 \quad [36]$$

Based on the physical processes governing behavior, various other forms of CVI may also be simulated by modifying the appropriate boundary conditions. For example, by disabling the EM module and dropping the energy balance equation (Eq. 12) altogether, isothermal CVI may be simulated. Similarly, the model may readily be adapted for simulating other forms of CVI, including forced-flow CVI and pressure-pulsed CVI by modifying the pressure boundary condition, Eq. 35.

Numerical Method of Solution

The numerical method used to solve the governing equations must be general enough to be able to describe the geometry of the metallic chamber and the coil configuration for induction heating. Furthermore, since one of the primary advantages of CVI with RF heating is the ability to infiltrate preforms of complicated geometry, the numerical technique should also be capable of describing arbitrary preform geometries. Therefore, a finite-element formulation was used to solve the governing equations.

The finite element method²³ involves the discretization of the problem domain into a finite number of elements. Within each element, the spatial distribution of the vari-

ous degrees of freedom, δ^e , is approximated by piecewise continuous polynomials of the form

$$\delta^h(r, z) = \{\mathbf{N}(r, z)\}^T \{\delta^e\} \quad [37]$$

where $\{\mathbf{N}(r, z)\}$ represents the vector of element approximation functions. In this work, isoparametric bilinear quadrilateral elements were employed. The Galerkin method requires the weak formulation of the governing equations. Approximations of the form shown in Eq. 37 are then substituted to give a set of element equations. The element equations are assembled with the appropriate boundary conditions to produce the discretized form of the governing equations.

The domain of the EM module consists of the entire volume within the metallic chamber. Only the right half of the r - z plane need be considered for discretization due to azimuthal symmetry. Further, since capacitive losses are negligible for the present case study, the current is constant all along the coil, and the problem acquires axial symmetry. Thus, only the upper-right quadrant of the r - z plane is required to model the entire chamber. Due to similar symmetry considerations, the domain of the CVI module consists only of the upper-right quadrant of the preform. For convenience, the finite element mesh for the EM and CVI modules were selected so as to coincide in the preform. The finite-element mesh used to obtain the numerical solution is shown in Fig. 2.

The Galerkin finite-element formulation for E_θ from Eq. 7 yields the discretized form

$$[K_E]\{\delta_E\} = \{f_E\} + \{P_E\} \quad [38]$$

which constitutes a set of linear complex algebraic equations. These equations were solved directly using a complex matrix solver. In order to solve for the dependent variables T , x_1, \dots, x_{N_c-1} , p , and ϵ , Eq. 12, 16, 18, and 31 were discretized to give a set of nonlinear implicit ordinary differential equations (ODEs) of the form

$$[C]\{\dot{\delta}\} + [K]\{\delta\} = \{f\} + \{P\} \quad [39]$$

This set of ODEs was solved using LSODI, a variable order, variable time-step, implicit ODE integrator based on backward-difference formulas.²⁴ The EM module was called at every function evaluation in the ODE integrator, thus preserving the coupling between the electric field in the preform and porosity evolution. Further details of the model and its numerical implementation are available in Ref. 25.

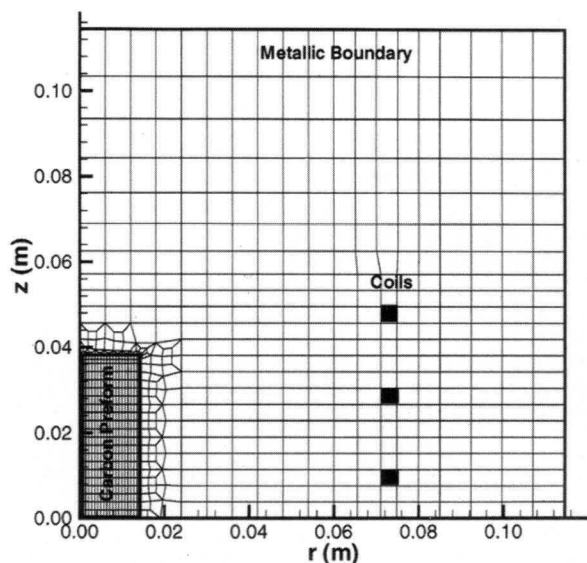


Fig. 2. Finite-element mesh used for numerical simulations.

Results and Discussion

The values of the parameters used in the simulation are shown in Table I. CVI involves several physical phenomena occurring at disparate time scales. Table II shows the order of magnitude of the different time scales. Based on these time scales, the overall behavior may be divided into two regimes.

1. Short time response ($t \ll 1$ h), which includes the period in which significant densification has not occurred in the preform and the temperature profiles evolve only due to induction heating, with the preform material properties being at their initial values.

2. Long time response ($t \gg 1$ h), when densification of the preform causes significant changes in the material properties, becoming the dominant mechanism for further evolution of the temperature and concentration profiles.

Short time response.—By comparing the characteristic time scale for heat transfer with the time period for harmonic oscillations of the electromagnetic fields, it is clear that the preform temperature will respond only to the time-averaged value of the power deposited by the fields. This justifies the solution of the electric fields in the frequency domain (Eq. 7) as opposed to the time domain.

Figure 3a shows initial profiles of the modulus of the electric field in the chamber enclosed by the metallic boundary. The azimuthal electric field is zero at the center due to symmetry and peaks at the induction coil. For the parameters given in Table I, the penetration depth of the electric field is comparable to the radius of the preform. Some axial variation in the electric field exists which depends on the axial extent of the coil relative to the preform. Figure 3b shows the time-averaged values of power density deposited in the preform by the RF field. At early times, the power density profiles simply mirror the profiles of the electric field, since the initial preform density (and conductivity) is uniform. Simulated results of the electric field and power deposition (Fig. 3) show excellent agreement with an existing electromagnetic solver,²⁰ which is based on a finite-difference formulation of Maxwell's equations.

Since the characteristic diffusion time scale is significantly less than the heat-transfer time scale, the reactant gas (methane) is able to diffuse into the preform while the preform is still relatively cool. That way the reactant concentration within the preform becomes equal to the bulk concentration with negligible product formation. As the preform temperature increases, reaction starts to take place and concentration gradients are established.

As energy is deposited into the volume of the preform by the electric fields, Fig. 4 shows the formation of a peak in

Table I. Parameter values used in the simulation.

Preform radius	0.0142 m
Preform height	0.0762 m
Initial porosity	0.70
Heat-transfer coefficient	10 W/m ² K
Carbon thermal conductivity	15 W/m K
Carbon specific heat	0.675 kJ/kg K
Carbon density	2270 kg/m ³
Emissivity	0.86
Frequency	50 kHz
Carbon electrical conductivity	5×10^4 S/m
Total power	4 kW
Initial pressure	1.01×10^4 Pa
Initial pore radius	40 μ m
Ambient temperature	300 K
Ambient CH ₄ mole fraction	0.6
Ambient Ar mole fraction	0.4

Table II. Time scales of physical phenomena involved in CVI.

Electromagnetic	1/f	0.0001 s
Mass transfer	R^2/D	0.1 s
Heat transfer	$(R^2 \rho C_p)/k^e$	10 s
Solid deposition	$\rho_s/(M_s C k_1)$	1000 s

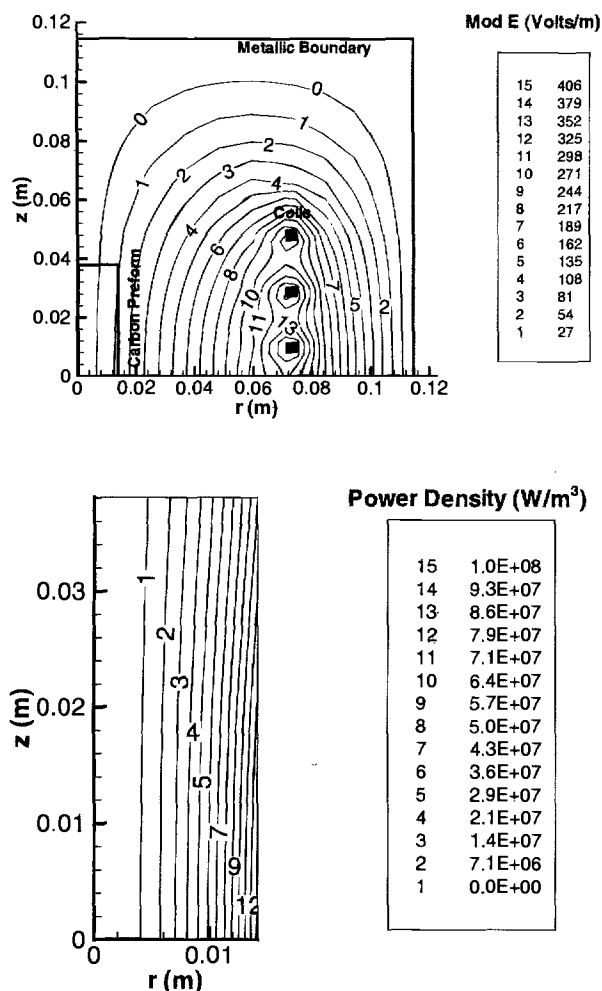


Fig. 3. (a, top) Initial distribution of the modulus of the electric field in the chamber and (b, bottom) initial power density distribution in the volume of the preform.

the temperature profiles representing an accumulation of energy. Since the maximum power is deposited at the edge of the preform with cooling at the external boundaries, this peak is initially formed near the edge and then gradually migrates toward the center of the preform. Heat loss occurs initially due to convection but is soon dominated by radiation as the temperature of the preform rises. After a

few minutes, a pseudosteady state is attained with the maximum temperature at the center of the preform (on axis). This temperature profile is maintained till significant densification commences in the preform.

The temperature distribution with volumetric heating presents an inherent advantage compared to isothermal CVI. The temperature gradients favor the densification in the interior of the preform with relatively little reaction at exterior surfaces, which remain at a lower temperature. Volumetric heating, therefore, favors an "inside-out" densification of the preform. In contrast, since the boundaries are at a relatively high temperature in isothermal CVI, densification at the boundaries causes diffusional limitations for the reactant.

Long time response.—For the first few hours of the process, reactant (methane) diffuses into the preform without significant diffusional limitations and densification occurs predominantly in the center of the preform, as dictated by the temperature distribution. However, key material properties governing the infiltration process change with densification and alter the subsequent densification pattern. Such material properties include the effective electrical and thermal conductivity, and the effective mass diffusivities of the chemical species within the preform. Figures 5 through 8 show the evolution of the profiles for power density, temperature, reactant concentration, and porosity within the preform for relatively long times.

With densification of the preform, the effective electrical conductivity of the material increases, see Eq. 9. This reduces the penetration depth of the electric field and alters the power deposition profile in the preform. The power density (Fig. 5) shows the formation of a sharp peak at the edge of the preform, near $z = 0$, where significant densification has occurred (Fig. 8). Since the total power deposited in the preform is kept constant, the power density at the ends of the preform ($z = L$) decreases during this period to compensate for the formation of the peak. The magnitude of the peak decreases as the region with high power density expands with densification of the preform. Since the energy absorbed by the preform is a function of both the power density and the volume of solid (Eq. 12), the net result is a significant increase in energy absorption by the central region of the preform.

The coupling between the absorbed energy and the densification process has important ramifications on the densification pattern. Densification causes more power to be absorbed by the body in regions of higher mass density, leading to further densification and more power absorption. This behavior constitutes a thermal runaway mechanism. Con-

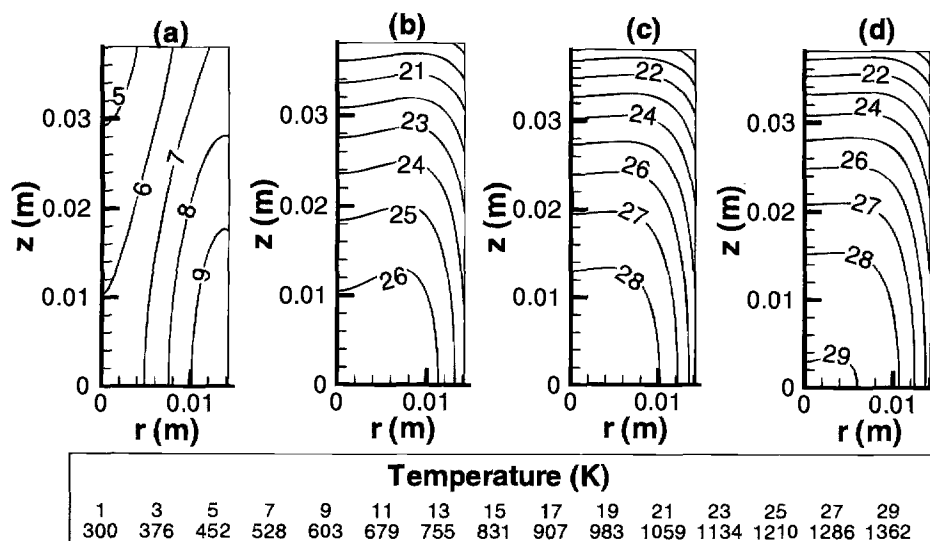


Fig. 4. Temperature distribution in the preform for short-time scales: (a) 3.6, (b) 18.0, (c) 28.8, and (d) 36.0 s.

sequently, the overall temperature at the center of the body increases with densification, as shown in Fig. 6. The feedback mechanism is alleviated only by the correspond-

ing decrease in the coil current for maintaining constant total power within the preform, thereby averting a complete thermal runaway.

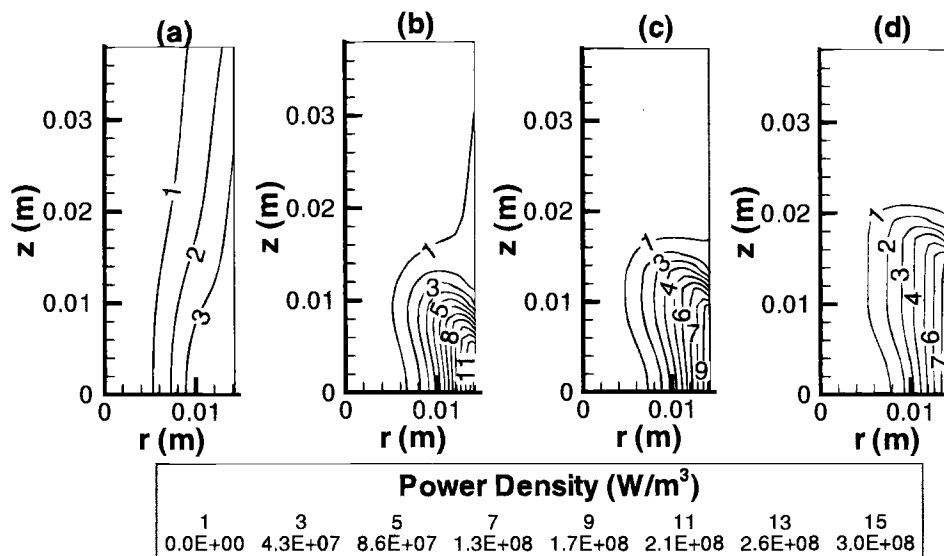


Fig. 5. Evolution of power density in the volume of the preform for long time scales: (a) 1, (b) 5, (c) 15, and (d) 100 h.

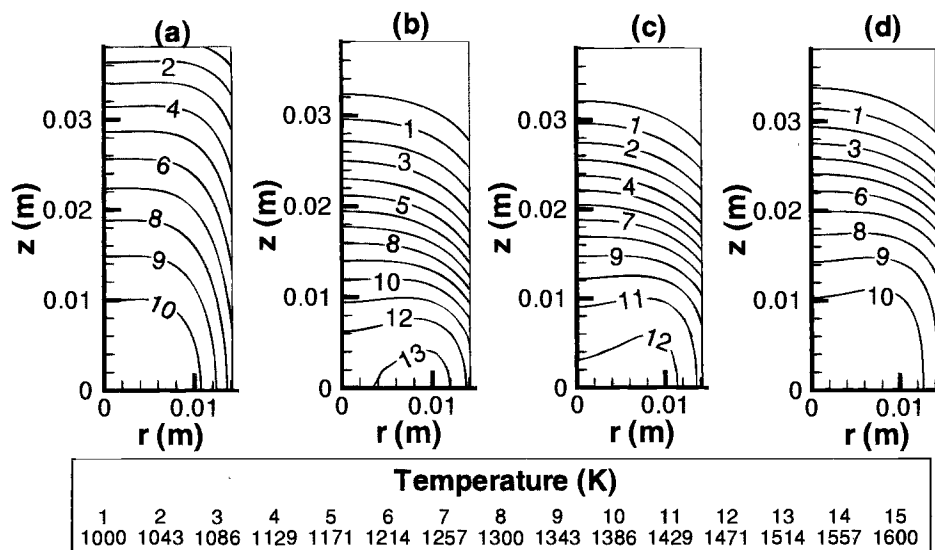


Fig. 6. Evolution of preform temperature for long time scales: (a) 1, (b) 5, (c) 15, and (d) 100 h.

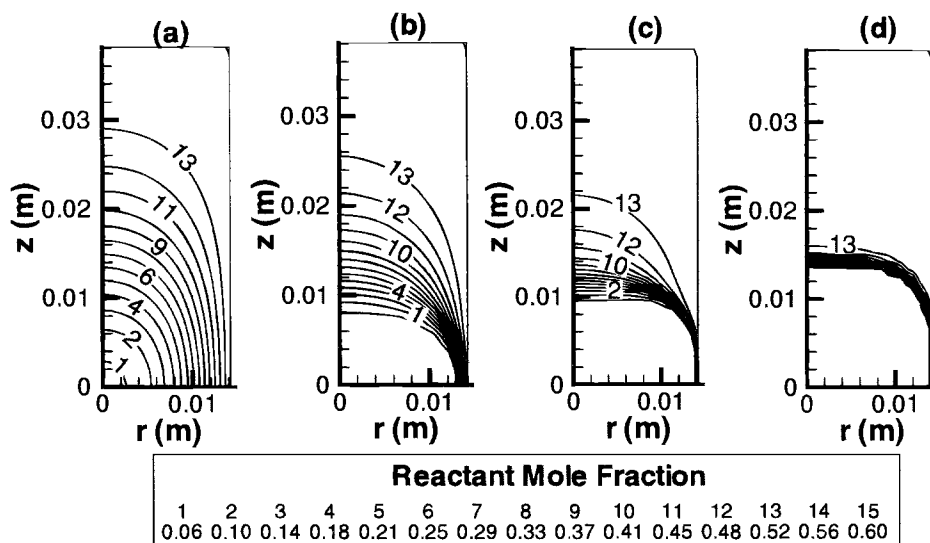


Fig. 7. Evolution of reactant mole-fraction for long time scales: (a) 1, (b) 5, (c) 15, and (d) 100 h.

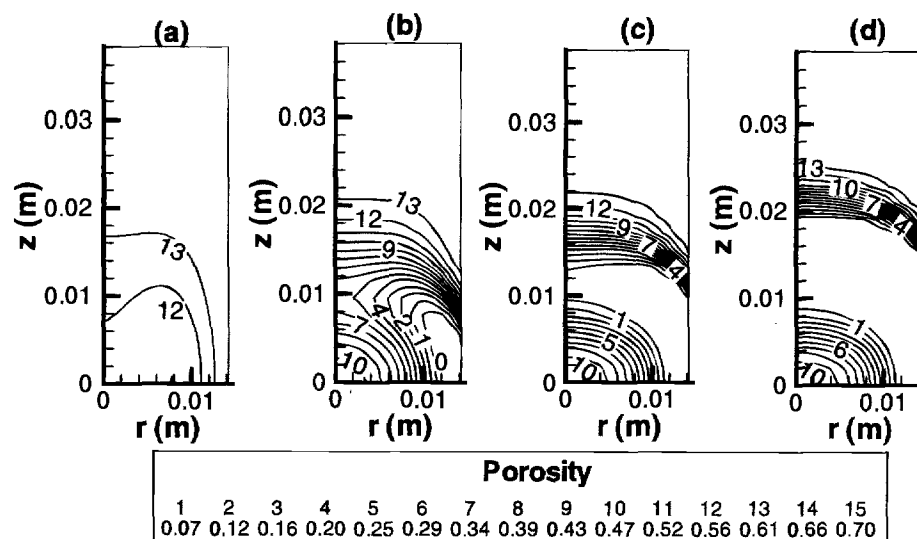


Fig. 8. Evolution of preform porosity for longtime scales: (a) 1, (b) 5, (c) 15, and (d) 100 h.

As discussed earlier, the absorbed energy is conducted to the edges ($r = R$) and the two ends ($z = L$) of the preform where it is lost to the surroundings by radiation. The evolving power distribution profile causes the formation of an off-axis peak in the temperature near the center of the preform ($z = 0$). The peak temperature rises from 1400 (Fig. 4) to 1600 K (Fig. 6) during the initial stages of the densification process. However, as the thermal conductivity of the material increases with densification, heat is conducted at a faster rate from the hotter regions of the body to the cooler regions. There is an overall decrease in the temperature gradients within the body with smaller gradients in the radial direction than the axial direction due to the preform geometry (aspect ratio). Consequently, the peak temperature at the center of the preform first increases and then decreases as the preform densifies.

The rate of decomposition of methane increases as the temperature of the preform rises causing more deposition of carbon within the pores. The effective diffusivity of methane decreases as the pore size decreases, leading to steep concentration gradients in the axial and radial directions (Fig. 7). Eventually, the reactant concentration profiles dominate the densification process and the region of maximum densification migrates radially from the center toward the edges (Fig. 8). At that time, the temperature at the edges is high enough to ensure that reaction occurs only at the edges of the preform exposed to the reactant. This effectively seals off the edges and causes the formation of entrapped porosity in the interior of the preform.

As the edges of the preform get plugged, further densification occurs mainly in the axial direction. The axial ends of the preform remain relatively cool and are easily accessible by the reactant. The overall densification process, therefore, proceeds in an "inside-out" manner initially in the radial direction and subsequently in the axial direction. Clearly, the overall geometry plays an important role during the densification of the preform. These geometrical effects are neglected in simple 1D models of CVI.

Simulation results showed a final average porosity of 0.04 corresponding to a preform density of 1.9 g/cm³. The entrapped porosity in the center of the preform contributes little to the overall porosity but may have a significant impact on the mechanical properties of the material. Thus, the overall change in bulk density, as is commonly reported in experimental studies, may not be the best criterion for assessing the success of the infiltration process for multidimensional preforms.

The origin of the entrapped porosity in the interior of the preform is the thermal runaway mechanism resulting in premature plugging of pores at the radial edge of the preform. The entrapped porosity may be reduced by decreasing the power from the induction coil. However,

this results in a significant increase in processing time. The runaway mechanism itself cannot be used for heating the preform since a minimum preform temperature is necessary to initiate the methane decomposition reaction. Therefore, power modulation schemes similar to those suggested by Morell *et al.*^{10,11} may become necessary, especially if scale-up of the process to larger preforms is desired.

Comparison with experimental data.—Most theoretical CVI studies reported in the literature so far do not compare predictions with experimental data. Limited experimental data for CVI with RF heating exists in the literature for direct comparison with simulations. The recent experimental study by Devlin *et al.*⁹ reports the infiltration of a 3 in. long by 1 in. diam carbon preform with a maximum power of 6 kW. Overall densities of 1.7 g/cm³ were achieved in 30 h of infiltration. The preform temperature ranged from 1400 to 1600 K, which compares favorably with calculated values from the model (see Fig. 6). The experiments also showed an increase in temperature with densification of the preform which confirms the thermal runaway mechanism identified in the simulation.

The radial distribution of temperature in the preform was monitored in the experiments at three radial locations on the $z = 0$ plane: the center of the preform, approximately halfway from the center to the edge, and near the edge of the preform. Although the absolute values of the three different temperatures were not reported, the temperature difference between the center and the edge was reported as a function of time. The temperature difference peaked at a value of 180 K after 3 h of infiltration and then decreased steadily to about 60 K after 13 h of infiltration.

Figure 9 shows the simulated value of the difference between the center temperature ($r = z = 0, T_0$) and edge temperature ($r = R, z = 0, T_{1,0}$) as a function of time for the parameters in Table 1. The simulated results show the formation of a peak similar to the experimental measurements. The behavior of the temperature gradient may be understood by comparing the rate of heat conduction within the preform to the rate of heat loss to the surroundings. Once densification of the preform is initiated, more power is deposited near the center ($z = 0$) than the ends of the preform. The temperature at the center of the preform rapidly increases, leading to greater radiation losses from the edges. Heat losses are dominated by radiation and increase nonlinearly with the preform surface temperature. This behavior tends to increase the temperature gradients in the preform with time. However, as the preform densifies, the effective value of the thermal conductivity increases, leading to a decrease in the temperature gradients within the preform. This becomes apparent by comparing the temperature difference profile to that of

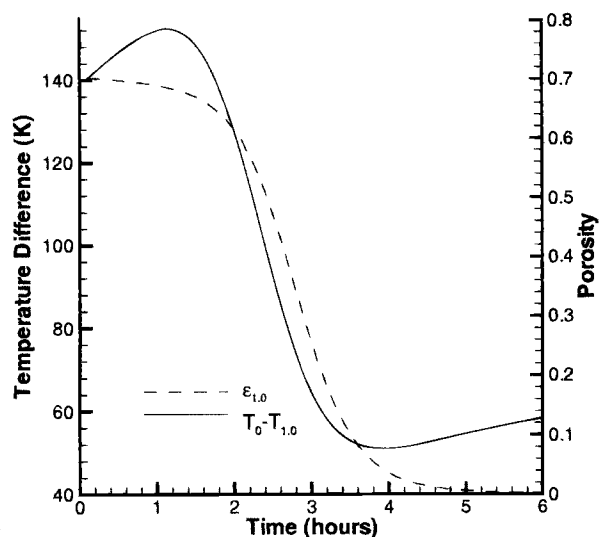


Fig. 9. Time evolution of the difference in temperature between the center and radial edge of the preform at the $z = 0$ plane, T_c is the center temperature and $T_{1,0}$ the edge temperature. The edge porosity $\epsilon_{1,0}$ is also shown as a function of time.

the edge porosity ($\epsilon_{1,0}$) in Fig. 9. Therefore, the temperature difference between the center and edge peaks and then decreases with densification.

Experiments⁹ also confirmed the formation of an off-center maximum in the radial temperature profile; the middle thermocouple showed a temperature 20 K higher than the center thermocouple. Figure 10 shows simulated values of the radial temperature profile during the densification process at $z = 0$. The simulations predict an off-axis peak in the radial temperature distribution once densification is initiated at the center of the preform. The formation of the peak signifies an increase in axial heat conduction compared to radial heat conduction. This is a direct consequence of the altered axial distribution of power density. Less power is deposited at the ends of the preform, favoring lower temperatures and greater axial heat conduction from the center. The magnitude of the peak diminishes with further densification as the effective thermal conductivity of the material increases. Other conditions leading to the formation of an off-axis peak in the temperature profiles may also be envisioned.

1. The thermal conductivity of the composite may be anisotropic with higher conductivity in the axial direction compared to the radial direction. This may cause an off-axis radial peak due to more efficient cooling from the axial ends of the preform.

2. The effective electrical conductivity of the composite increases not only due to changing porosity (which is accounted in the simulation) but also due to temperature. Then the electric field penetration depth may become much smaller than the radius (and the length of the preform). Power would be deposited mainly at the corners of the preform and heat losses from the ends of the preform could produce an off-axis maximum in the temperature profiles.

Modeling of this behavior requires, at the very least, a two-dimensional description of temperature and power density distribution and again underlines the importance of 2D models *vs.* simplified 1D models.

The overall trends predicted by the model are similar to the experimental results. However, the predicted value of processing time is about 180 h for a power input of 4 kW, resulting in a final density of 1.9 g/cm³. Experimentally, processing times of the order of 30 h for 6 kW power input were reported, resulting in a final density of 1.7 g/cm³.⁹ Also, the predicted peak in the temperature difference *vs.* time (Fig. 9) is only about 160 K, whereas measured values were closer to 180 K. Direct quantitative comparison with

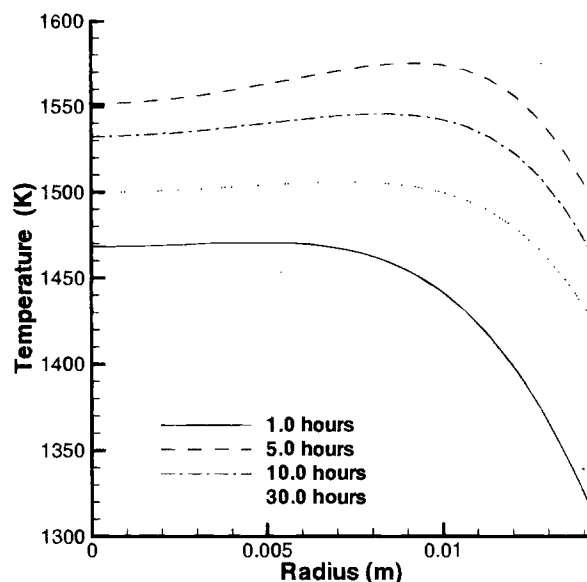


Fig. 10. Time evolution of the radial temperatures profile at the $z = 0$ plane.

the experimental data is difficult because the actual geometrical dimensions of the experiment (*e.g.*, location of coil) are not known and more important, because of uncertainty in the physical and transport properties of the preform. It is clear from the discussion of Fig. 5 through 8 that properties such as the effective electrical and thermal conductivity play a critical role. Only estimates of these properties²⁶ were used in the simulation. More important, the evolution of these properties with changing preform porosity and temperature has a significant impact on the overall densification behavior. Various other properties such as the effective surface area and emissivity for radiation also affect the energy balance in the preform and may change as the surface temperature changes. Finally, the reaction kinetics used was greatly simplified. Current work is directed toward examining the parametric sensitivity of important results and incorporating improved models for material properties.

Summary and Conclusions

A comprehensive 2D model for chemical vapor infiltration with RF heating was developed. The model consisted of an electromagnetics (EM) module solving Maxwell's equations coupled self-consistently with a CVI module for the description of multicomponent transport and reaction phenomena in a porous preform. As an application study, the model was used to simulate the densification of a cylindrical carbon preform keeping a constant total power absorption. Densification of the preform proceeded in an "inside-out" pattern, first in the radial direction and then in the axial direction. This indicates that the 2D geometry of the preform plays an important role, which cannot be captured by simpler 1D models reported in the literature.

A thermal runaway mechanism with RF heating was identified which results in increasing temperature as the preform densifies. This runaway could cause entrapment of porosity in the interior of the preform and adversely affect the mechanical properties of the final product. Power modulation schemes (pulsed-power) may help avert the thermal runaway.

The simulation results predicted semi-quantitatively important trends shown in experiments, including the formation of an off-axis peak in the radial temperature distribution. However, for better quantitative agreement with the data, more experimental details and the dependence of material properties on temperature, frequency, and porosity are required.

The proposed model is based on fundamental principles of EM wave propagation and absorption, energy transport, multicomponent mass transport, and chemical reaction

kinetics. As such, the model provides a sound basis for examining scale-up to larger preforms and the development of improved CVI processes such as RF heating with power modulation, RF heating with forced flow, or RF heating with pressure-pulsing.

Acknowledgments

This work was supported financially by a SRA/AFOSR contract and by the Energy Laboratory at the University of Houston.

Manuscript submitted March 13, 1997; revised manuscript received Aug. 4, 1997.

The University of Houston assisted in meeting the publication costs of this article.

LIST OF SYMBOLS

B	permeability of preform, m^2
c	speed of light, m/s
C	gas concentration, $kmol/m^3$
C_s	solid concentration, $kmol/m^3$
C_i	gas concentration of i th species, $kmol/m^3$
C_{pi}	heat capacity of the i th species, $J/(kg K)$
C_{ps}	heat capacity of solid, $J/(kg K)$
$D_{i,ps}$	effective Knudsen diffusivity of the i th species, m^2/s
D_{ij}^0	binary diffusivity of the i - j pair, m^2/s
e	emissivity
E	electric field, V/m
E_i	reaction activation energy, $J/kmol$
E_θ	azimuthal component of electric field, V/m
H	magnetic field, H/m
J^i	impressed current density, A/m^2
J_i	diffusive molar flux of the i th species, $kmol/m^2 s$
k_i	reaction rate constant, $1/s$
k_c^e	effective thermal conductivity, $W/(m K)$
\bar{K}	relative permittivity
K_c	complex relative permittivity
M_s	solid molecular weight, $kg/kmol$
n	unit vector normal to surface
$\{N\}$	vector of finite element approximation functions
N_H	heat flux, W/m^2
N_i	molar flux of the i th species, $kmol/(m^2 s)$
N_T	total molar flux, $kmol/(m^2 s)$
p	pressure, Pa
p_a	ambient pressure, Pa
r	radial coordinate, m
R	preform radius, m , and gas constant, $(kg m^3)/(s^2 kmol K)$
s	Stefan-Boltzmann constant, $W/(m^2 K^4)$
T	temperature, K
T_a	ambient temperature, K
\bar{W}	power density, W/m^3
x_i	mole fraction of the i th species
z	axial coordinate, m
Greek	
δ	degree of freedom
ϵ_0	dielectric constant of free space, F/m , and initial preform porosity
ϵ	preform porosity

μ_0	magnetic permeability of free space, H/m
ρ_s	solid density, kg/m^3
σ	electrical conductivity, S/m
ω	angular frequency, rad/s

REFERENCES

- D. P. Stinton, R. A. Lowden, and T. M. Besmann, *Mater. Res. Soc. Symp. Proc.*, **250**, 233 (1992).
- T. L. Starr, *ibid.*, **250**, 207 (1992).
- D. J. Devlin, R. P. Currier, R. S. Barbero, B. F. Espinoza, and N. Elliot, *ibid.*, **250**, 233 (1992).
- K. Sugiyama and Y. Ohzawa, *J. Mater. Res.*, **25**, 4511 (1990).
- I. Golcecki, R. C. Morris, D. Narasimhan, and N. Clements, *Ceram. Eng. Sci. Proc.*, **16**, 315 (1995).
- I. Golcecki, R. C. Morris, D. Narasimhan, and N. Clements, *Appl. Phys. Lett.*, **66**, 2334 (1995).
- I. Golcecki, R. C. Morris, D. Narasimhan, and N. Clements, *Ceram. Eng. Sci. Proc.*, **16**, 315 (1995).
- I. Golcecki, R. C. Morris, D. Narasimhan and N. Clements, in *Chemical Vapor Deposition XIII*, T. M. Besmann, M. D. Allendorf, McD. Robinson, and R. K. Ulrich, Editors, PV 96-5, p. 547, The Electrochemical Society Proceedings Series, Pennington, NJ (1996).
- D. J. Devlin, R. S. Barbero, and K. N. Siebein, *ibid.*, p. 571.
- D. Gupta and J. W. Evans, *J. Mater. Res.*, **6**, 810 (1991).
- J. I. Morell, D. J. Economou, and N. R. Amundson, *This Journal*, **139**, 328 (1992).
- J. I. Morell, D. J. Economou, and N. R. Amundson, *J. Mater. Res.*, **7**, 2447 (1992).
- J. I. Morell, D. J. Economou, and N. R. Amundson, *ibid.*, **8**, 1067 (1993).
- S. M. Gupta and J. A. Tsamopoulos, *This Journal*, **137**, 1626 (1990).
- N. H. Tai and T. W. Chou, *J. Am. Ceram. Soc.*, **73**, 1489 (1990).
- N. H. Tai, T. W. Chou, and C. C. M. Ma, *ibid.*, **77**, 849 (1994).
- S. V. Sotirchos, *AIChE J.*, **37**, 1365 (1991).
- C. A. Balanis, *Advanced Engineering Electromagnetics*, John Wiley & Sons, New York (1989).
- S. Ramo, J. R. Whinnery, and T. V. Duzer, *Fields and Waves in Communication Electronics*, John Wiley & Sons, New York (1993).
- E. F. Jeager, L. A. Berry, J. S. Tolliver, and D. B. Batchelor, *Phys. Plasmas*, **2**, 2597 (1995).
- R. Jackson, *Transport in Porous Catalysts*, Elsevier Publishing Company, New York (1977).
- R. B. Bird, W. E. Stewart, and E. N. Lightfoot, *Transport Phenomena*, John Wiley & Sons, New York (1960).
- T. J. R. Hughes, *The Finite Element Method*, Prentice-Hall, Englewood Cliffs, NJ (1987).
- A. C. Hindmarsh, *ACM-SIGNAL Newsletter*, **15**, 10 (1980).
- V. Midha, Ph.D. Thesis, University of Houston, Houston, TX, In progress.
- R. H. Perry and D. Green, *Perry's Chemical Engineers' Handbook*, 6th ed., McGraw-Hill Book Co., Singapore (1984).